



**HAL**  
open science

## Libration-induced Orbit Period Variations Following the DART Impact

Alex J. Meyer, Ioannis Gkolias, Michalis Gaitanas, Harrison F. Agrusa, Daniel J. Scheeres, Kleomenis Tsiganis, Petr Pravec, Lance A. M. Benner, Fabio Ferrari, Patrick Michel

► **To cite this version:**

Alex J. Meyer, Ioannis Gkolias, Michalis Gaitanas, Harrison F. Agrusa, Daniel J. Scheeres, et al.. Libration-induced Orbit Period Variations Following the DART Impact. *The Planetary Science Journal*, 2021, 2, 10.3847/PSJ/ac3bd1 . insu-03656931

**HAL Id: insu-03656931**

**<https://insu.hal.science/insu-03656931>**

Submitted on 2 May 2022

**HAL** is a multi-disciplinary open access archive for the deposit and dissemination of scientific research documents, whether they are published or not. The documents may come from teaching and research institutions in France or abroad, or from public or private research centers.

L'archive ouverte pluridisciplinaire **HAL**, est destinée au dépôt et à la diffusion de documents scientifiques de niveau recherche, publiés ou non, émanant des établissements d'enseignement et de recherche français ou étrangers, des laboratoires publics ou privés.



Distributed under a Creative Commons Attribution 4.0 International License



# Libration-induced Orbit Period Variations Following the DART Impact

Alex J. Meyer<sup>1</sup> , Ioannis Gkolias<sup>2</sup> , Michalis Gaitanas<sup>2</sup>, Harrison F. Agrusa<sup>3</sup> , Daniel J. Scheeres<sup>1</sup> , Kleomenis Tsiganis<sup>2</sup> ,  
Petr Pravec<sup>4</sup> , Lance A. M. Benner<sup>5</sup>, Fabio Ferrari<sup>6</sup>, and Patrick Michel<sup>7</sup> 

<sup>1</sup> Smead Department of Aerospace Engineering Sciences, University of Colorado Boulder, Boulder, CO 80303, USA; [alex.meyer@colorado.edu](mailto:alex.meyer@colorado.edu)

<sup>2</sup> Department of Physics, Aristotle University of Thessaloniki, GR 54124 Thessaloniki, Greece

<sup>3</sup> Department of Astronomy, University of Maryland, College Park, MD 20742, USA

<sup>4</sup> Astronomical Institute of the Czech Academy of Sciences, Fričova 1, CZ-25165 Ondřejov, Czech Republic

<sup>5</sup> Jet Propulsion Laboratory, California Institute of Technology, Pasadena, CA 91109-8099, USA

<sup>6</sup> Space Research and Planetary Sciences, Universität Bern, Gesellschaftsstrasse 6, 3012 Bern, Switzerland

<sup>7</sup> Université Côte d'Azur, Observatoire de la Côte d'Azur, CNRS, Laboratoire Lagrange, CS34229, F-06304 Nice Cedex 4, France

Received 2021 September 10; revised 2021 November 18; accepted 2021 November 19; published 2021 December 15

## Abstract

The Double Asteroid Redirection Test (DART) mission will be the first test of a kinetic impactor as a means of planetary defense. In late 2022, DART will collide with Dimorphos, the secondary in the Didymos binary asteroid system. The impact will cause a momentum transfer from the spacecraft to the binary asteroid, changing the orbit period of Dimorphos and forcing it to librate in its orbit. Owing to the coupled dynamics in binary asteroid systems, the orbit and libration state of Dimorphos are intertwined. Thus, as the secondary librates, it also experiences fluctuations in its orbit period. These variations in the orbit period are dependent on the magnitude of the impact perturbation, as well as the system's state at impact and the moments of inertia of the secondary. In general, any binary asteroid system whose secondary is librating will have a nonconstant orbit period on account of the secondary's fluctuating spin rate. The orbit period variations are typically driven by two modes: a long period and a short period, each with significant amplitudes on the order of tens of seconds to several minutes. The fluctuating orbit period offers both a challenge and an opportunity in the context of the DART mission. Orbit period oscillations will make determining the post-impact orbit period more difficult but can also provide information about the system's libration state and the DART impact.

*Unified Astronomy Thesaurus concepts:* Asteroid dynamics (2210); Asteroid satellites (2207); Celestial mechanics (211); Orbital evolution (1178)

## 1. Introduction

The Double Asteroid Redirection Test (DART) is NASA's first planetary defense mission and part of the Asteroid Impact and Deflection Assessment (AIDA) collaboration (Cheng et al. 2018). AIDA is an international collaboration between NASA and ESA, with the purpose of investigating the viability of a kinetic impactor as a means of deflecting a potentially hazardous asteroid (Cheng et al. 2015). The target is the Didymos binary asteroid system, consisting of the primary asteroid Didymos and its smaller secondary moon, Dimorphos. DART will impact Dimorphos as it orbits Didymos, thereby changing the mutual orbital period within the binary asteroid system. The change in orbit period will be measured from ground-based observations in order to calculate the total momentum transferred to the Didymos system. The ground-based observations will be combined with data from LICIA-Cube, a CubeSat carried by DART that will jettison just before impact and observe the collision up close (Dotto et al. 2021). DART will be followed by Hera, ESA's contribution to AIDA launching in 2024. Hera will rendezvous with the Didymos system in 2026 to complete a post-impact survey (Tsiganis et al. 2019; Michel et al. 2021). Additionally, Hera will carry two CubeSats, Juventas and Milani, that will aid in the study of the Didymos system, including probing for the first time the internal and subsurface properties, and ultimately attempt

landings on Dimorphos (Goldberg et al. 2019; Ferrari et al. 2021).

Binary asteroids are common among near-Earth asteroids, composing at least 15% of these bodies (Pravec et al. 1999, 2006). Binary asteroids are formed by spin-up and fission caused by solar torque of the primary (Walsh et al. 2008; Jacobson et al. 2013), and their evolution is then dominated by tidal forces (Taylor & Margot 2010, 2014) and the BYORP effect (Čuk & Burns 2005; Čuk & Nesvorný 2010; Steinberg & Sari 2011). Tidal forces cause the binary system to expand, while BYORP can either expand or contract the system. Stable binary systems arise when these mechanisms are balanced (Jacobson & Scheeres 2011). In these systems, the primary rotates rapidly and the secondary is tidally locked in a 1:1 spin-orbit resonance. In this work, we assume that Didymos is in such an equilibrium. This equilibrium can be disrupted by close planetary encounters (Meyer & Scheeres 2021).

The relevance of binary asteroids has increased recently owing to the interest in these systems as mission targets. Beyond DART, Lucy is visiting the Trojan asteroids (Levison et al. 2017), including two binary asteroid pairs (Levison et al. 2021). Janus is another mission targeting binary asteroids, also visiting two systems (Scheeres et al. 2020). This recent uptick in interest can be attributed to the unique advantages binary asteroids provide. Binary asteroids offer an ideal test bed for planetary defense missions owing to their fast dynamics (Cheng et al. 2018), meaning that changes in the system are visible from the ground. Binary asteroids also offer new opportunities to study tidal forces and solar radiation torques, since these effects dominate their evolution.

When DART impacts Dimorphos, it will transfer momentum to the Didymos system. This momentum transfer is captured by the momentum enhancement factor  $\beta$ , which is the ratio of the total momentum transferred to the momentum transferred by a perfectly inelastic collision (Cheng et al. 2015). This captures the effect that ejecta from the surface of Dimorphos will have on the overall momentum transfer. Thus, the minimum value of  $\beta$  is 1, corresponding to an inelastic collision with no ejecta and the sole transfer of momentum from the spacecraft to the asteroid. The true value of  $\beta$  will be larger than 1 and dependent on the properties of Dimorphos.

The predicted effects of the DART impact have been studied in depth. Agrusa et al. (2020) showed that the dynamics within the Didymos system are strongly coupled and non-Keplerian, typical of binary asteroids. Additionally, they demonstrated that the DART impact will likely induce significant libration in the secondary. Agrusa et al. (2021) further examined the induced libration and pointed out instabilities caused by resonances between the libration frequencies and the mean motion. Additional impact simulations were carried out by Fahnestock et al. (2018) to predict the induced libration amplitude post-impact. The Didymos system has also been studied by radar observations to obtain a shape model of the primary, along with estimates of the system mass and secondary shape (Naidu et al. 2020). Meanwhile, photometric observations have provided constraints on the orbit and spin pole of Didymos (Scheirich et al. 2019; Thomas et al. 2021).

Binary asteroids such as Didymos are modeled by the full two-body problem (F2BP), in which the rotational and orbital motions of the bodies are coupled together (Scheeres 2002). The coupling is due to the close proximity of the two asteroids, along with their generally asymmetric shapes. The equations of motion for the F2BP were developed by Maciejewski (1995) and further studied by Scheeres (2006), Tricarico (2008), and Scheeres (2009), among others. Later, McMahon & Scheeres (2013) studied the libration in a coupled system that serves as the basis for this analysis. High-fidelity numerical simulations of binary asteroids in the F2BP were made possible by work done by Werner & Scheeres (2005), allowing for the use of polyhedral shape models in the equations of motion. Fahnestock & Scheeres (2006) used this method in an in-depth study of 1999 KW4 (now Moshup). Numerical efficiency was improved by the iterative algorithm developed by Hou et al. (2017) and implemented by Davis & Scheeres (2020) in the General Use Binary Asteroid Simulator (GUBAS) (Davis & Scheeres 2021). GUBAS is used extensively for the DART mission to model the dynamics of Didymos (Agrusa et al. 2020), and we will use it in this work to verify our results. GUBAS allows for the gravity field of polyhedron shape models to be truncated at a user-specified degree and order, usually fourth, in order to produce high-fidelity simulations of a binary asteroid.

While previous studies have characterized the coupled dynamics of Didymos (Hirabayashi et al. 2019; Agrusa et al. 2020; Naidu et al. 2020), they do not provide the complete picture. In particular, while the libration of Dimorphos has been studied extensively (Agrusa et al. 2021), the libration's effect on the orbit dynamics has not been investigated in the same level of detail. This analysis attempts to fill this gap by studying the libration and orbit dynamics together rather than separately. In order to do this, we rely on the work done by McMahon & Scheeres (2013), who lay the groundwork in examining the

**Table 1**

Parameters for the Nominal Didymos System (Pravec et al. 2006; Scheirich & Pravec 2009; Agrusa et al. 2020, 2021; Naidu et al. 2020)

Symbol	Parameter	Value	Source
$a_{\text{orb}}$	Orbit semimajor axis	$1.19 \pm 0.03$ km	Measured
$e_{\text{orb}}$	Orbit eccentricity	$<0.03$	Measured
$i_{\text{orb}}$	Orbit inclination	0.0	Assumed
$D_p$	Primary bulk diameter	$780 \pm 30$ m	Measured
$D_s$	Secondary bulk diameter	$164 \pm 18$ m	Derived
$M_{\text{sys}}$	System mass	$(5.37 \pm 0.44) \times 10^{11}$ kg	Derived <sup>a</sup>
$\nu$	Mass fraction	0.99	Derived
$P_{\text{orb}}$	Mutual orbit period	$11.9217 \pm 0.0002$ hr	Measured
$P_A$	Primary spin period	$2.2600 \pm 0.0001$ hr	Measured
$P_B$	Secondary spin period	$11.9217 \pm 0.0002$ hr	Assumed
$\rho$	System bulk density	$2170 \pm 350$ kg m <sup>-3</sup>	Derived <sup>a</sup>
$a/b$	Secondary major-axis ratio	1.3	Assumed <sup>b</sup>
$b/c$	Secondary minor-axis ratio	1.2	Assumed <sup>b</sup>
$m_{\text{DART}}$	Mass of DART	535 kg	Assumed
$v_{\text{DART}}$	Relative velocity of DART	$6.6$ km s <sup>-1</sup>	Assumed

**Notes.**

<sup>a</sup> Derived using Kepler's laws, so some error is expected.

<sup>b</sup> Assumed based on typical binary asteroid secondary shapes.

coupling between the libration and orbit dynamics. We use results from this study, combined with full numeric GUBAS simulations, to study the link between induced libration and apparent variations in the mutual orbit period. While the classical two-body problem expects a constant orbit period, this is not the case in the F2BP, where the rotation and translation of the bodies are coupled together. The libration of the secondary results in variations in the secondary's spin angular momentum as the secondary slows its rotation at the apex of its libration and speeds up as it passes through 0°. Furthermore, larger libration amplitudes result in larger variations in the spin angular momentum. In order to enforce the conservation of the system's angular momentum, the orbit angular momentum must also vary in response to the secondary's changing angular momentum. This variation in orbit angular momentum results in fluctuations in the orbit period.

The nominal pre-impact Didymos system and DART spacecraft parameters have been established by a variety of previous work in the literature and collected in Agrusa et al. (2020, 2021). Relevant parameters for this work are listed in Table 1 for convenience. These values will be used to define the DART spacecraft's mass and velocity and the pre-impact orbit of the Didymos system, unless otherwise noted in the analysis.

This work is organized as follows. First, we present a simplified, analytic dynamics model of a binary asteroid system to develop a link between the libration and orbit period in Section 2. Section 3 then uses this model, along with GUBAS simulations for verification, to study how the DART impact induces libration and, in turn, variations in the orbit period. In Section 4 we test over multiple levels of impact excitation and analyze the system's responses, considering uncertainties in the secondary's shape and configuration. We then relax our simplifications to simulate the full three-dimensional impact in Section 5, using asymmetric shape models. Section 6 discusses the implications of these results for the observation of Didymos

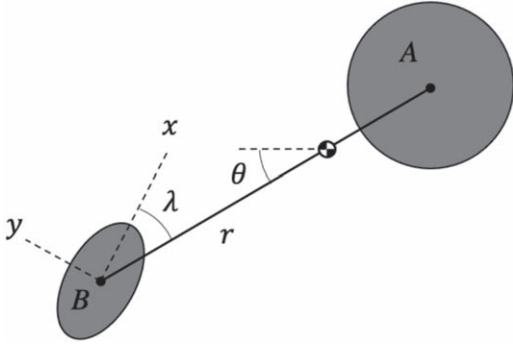


**Figure 1.** Top-down view of the simplified, planar model for the binary asteroid. The primary is body A, and the secondary is body B. In the singly synchronous configuration,  $\lambda$  is the libration angle.

and, by extension, other binary asteroid systems. We then discuss the results and provide brief conclusions in Section 7.

## 2. Dynamics Model

We first develop equations of motion for a simplified binary asteroid system following McMahon & Scheeres (2013). In the simplified system, we constrain the motion to be planar and model the primary as an oblate spheroid and the secondary as a triaxial ellipsoid. We nominally assume the secondary to be tidally locked pre-impact, as a result of enforcing equilibrium in the system. In this configuration, the long axis of the secondary is always pointing at the center of the primary, and its spin period is exactly equal to the orbit period. The impact will cause deviations from this equilibrium allowing for libration and, consequently, orbit period variations.

### 2.1. Equations of Motion

In developing equations of motion for the binary system dynamics, we approximate the primary as an oblate spheroid with moments of inertia  $I_{A,z} > I_{A,y} = I_{A,x}$  and the secondary as a triaxial ellipsoid with moments of inertia  $I_{B,z} > I_{B,y} > I_{B,x}$ . Here A refers to the primary and B to the secondary. In each of the body-fixed coordinate frames of the primary and secondary,  $x$  is the longest principal body-fixed axis,  $y$  is the intermediate principal body-fixed axis, and  $z$  is the shortest principal body-fixed axis. Since the primary is an oblate spheroid, for simplicity we define  $I_s = I_{A,y} = I_{A,x}$  as the equatorial moment of inertia of the axisymmetric primary. In this dynamics model, we assume that all orbital motion lies within the plane and that the poles of the primary, secondary, and mutual orbit are all aligned perpendicular to the plane of motion. An illustration of the system is shown in Figure 1, along with the relevant variables.

The full system's rotation in inertial space is measured by the angle  $\theta$ , and the separation of the two bodies' centers of mass is  $r$ . The orientation of the secondary relative to the rotating line  $r$  is measured by  $\lambda$ , which is also the libration angle. Due to the azimuthal symmetry of A, we do not concern ourselves with its rotation.

We normalize the system using the initial separation of the two bodies, denoted  $\alpha$ , and the mass of the secondary,  $m_B$ . The time is normalized using the mean motion of the system at the distance  $\alpha$ :  $n = \sqrt{G(m_A + m_B)\alpha^{-3}}$ . The system's mass fraction is defined as  $\nu = m_A(m_A + m_B)^{-1}$ , which is always greater than 0.5 and about equal to 0.99 in the nominal system (see

Table 1). The normalized inertia tensors are

$$\bar{I}_i = \frac{I_i}{m_i \alpha^2} \quad (1)$$

for body  $i$ , either A or B.

In order to develop full equations of motion, we define the potential energy of the system. Here we further simplify the system by only taking the second-order expansion of the potential energy. This is the identical expression used in McMahon & Scheeres (2013), so we will skip any derivation and directly report the result:

$$V(r, \lambda) = \frac{-\nu}{r} \left[ 1 + \frac{1}{2r^2} (\bar{I}_{A,z} - \bar{I}_s) - \frac{1}{2} \bar{I}_{B,x} - \frac{1}{2} \bar{I}_{B,y} + \bar{I}_{B,z} + \frac{3}{2} (\bar{I}_{B,y} - \bar{I}_{B,x}) \cos 2\lambda \right]. \quad (2)$$

The potential energy is used in the equations of motion, where we will again skip any derivation:

$$\ddot{r} = \dot{\theta}^2 r - \frac{1}{\nu} \frac{\partial V}{\partial r} \quad (3)$$

$$\ddot{\lambda} = - \left( 1 + \frac{\nu r^2}{\bar{I}_{B,z}} \right) \frac{1}{\nu r^2} \frac{\partial V}{\partial \lambda} + \frac{2\dot{r}\dot{\theta}}{r}. \quad (4)$$

In equilibrium, the mutual orbit is circular and the secondary is tidally locked. Thus, the equilibrium conditions are

$$\dot{r} = \ddot{r} = 0 \quad (5)$$

and

$$\lambda = \dot{\lambda} = \ddot{\lambda} = 0. \quad (6)$$

These conditions allow us to solve for the orbital rate at equilibrium:

$$\dot{\theta} = \sqrt{\frac{1}{\nu r} \frac{\partial V}{\partial r}}, \quad (7)$$

which is constant. Thus, at equilibrium (i.e.,  $0^\circ$  libration), the orbit period is constant.

### 2.2. Free Angular Momentum

Coupling between the libration of the secondary and the orbit period stems from the conservation of angular momentum. To investigate this, we assume that the spin angular momentum of the primary will be essentially unchanged by the DART impact. We turn to GUBAS numerical simulations to verify this assumption. Based on GUBAS simulations with a  $\beta$  factor equal to 3, the secondary's spin angular momentum changes by around 3.6%, while the orbital angular momentum changes by about 1.2% as a result of the impact. These changes are much larger compared to the primary's spin angular momentum change of around  $2 \times 10^{-4}\%$ , and thus we ignore any change in the primary's angular momentum. Despite the primary's large angular momentum, most of the change in momentum does indeed occur in the secondary and orbit. To investigate the momentum exchange, we define the free angular momentum as the total angular momentum minus the contribution by the primary:

$$H_{\text{free}} = H_{\text{total}} - H_A. \quad (8)$$

Under our assumption of constant primary angular momentum,  $H_{\text{free}}$  is constant in the absence of external perturbations. In the simplified system, the free angular momentum can be written as

$$H_{\text{free}} = \bar{I}_z \dot{\theta} + \bar{I}_{B,z} \dot{\lambda}, \quad (9)$$

where the system's mass-normalized polar moment of inertia is defined as

$$\bar{I}_z = \bar{I}_{B,z} + \nu r^2. \quad (10)$$

Note that the system polar inertia is a function of  $r$  and is thus not necessarily constant. We can rearrange this equation to get a direct relationship between the orbital rate and the libration rate:

$$\dot{\theta} = \frac{H_{\text{free}} - \bar{I}_{B,z} \dot{\lambda}}{\bar{I}_z}. \quad (11)$$

Equation (11) can be substituted into the equations of motion to eliminate  $\dot{\theta}$ :

$$\ddot{r} = \frac{(H_{\text{free}} - \bar{I}_{B,z} \dot{\lambda})^2 r}{\bar{I}_z^2} - \frac{1}{\nu} \frac{\partial V}{\partial r} \quad (12)$$

$$\ddot{\lambda} = - \left( 1 + \frac{\nu r^2}{\bar{I}_{B,z}} \right) \frac{1}{\nu r^2} \frac{\partial V}{\partial \lambda} + \frac{2\dot{r}(H_{\text{free}} - \bar{I}_{B,z} \dot{\lambda})}{r \bar{I}_z}. \quad (13)$$

McMahon & Scheeres (2013) also developed an expression for the separation distance required for equilibrium given a value of the free angular momentum. Here we simply invert this equation to solve for the free angular momentum required for a given separation distance to enforce equilibrium:

$$H^* = \left[ \frac{\nu^2}{r^5} \left( r^6 + \left[ \frac{2\bar{I}_{B,z}}{\nu} + \frac{3}{2} \bar{C}_I \right] r^4 + \left[ \frac{\bar{I}_{B,z}^2}{\nu^2} + \frac{3\bar{I}_{B,z} \bar{C}_I}{\nu} \right] r^2 + \frac{3\bar{I}_{B,z}^2 \bar{C}_I}{2\nu^2} \right) \right]^{\frac{1}{2}}, \quad (14)$$

where

$$\bar{C}_I = -2\bar{I}_{B,x} + \bar{I}_{B,y} + \bar{I}_{B,z} + \bar{I}_{A,z} - \bar{I}_s. \quad (15)$$

At this free angular momentum, all equilibrium conditions are met and the system is in a circular, tidally locked orbit with a given separation  $r$ .

### 2.3. Perturbation by the DART Impact

The DART impact will be retrograde, thus slowing the secondary in its orbit. When the spacecraft impacts Dimorphos, it will remove momentum from the system, thus perturbing the free angular momentum away from the equilibrium value. For a planar, head-on collision through the body's center of mass, we can define  $\beta$  as (Agrusa et al. 2021)

$$\beta = \frac{-m_B \Delta v}{m_{\text{DART}} v_{\text{DART}}}, \quad (16)$$

where  $\Delta v$  is the change in the secondary's orbital velocity and  $m_{\text{DART}}$  and  $v_{\text{DART}}$  are the mass and relative velocity of the DART spacecraft, respectively. The negative sign is a result of the retrograde impact, causing the secondary to slow in its orbit. Thus, the negative sign serves to keep the change in

velocity  $\Delta v$  positive for convenience. For this analysis, we assume a DART spacecraft mass of 535 kg and a relative velocity of  $6.6 \text{ km s}^{-1}$  (see Table 1).

Because we are assuming the impact to be head-on through the secondary's center of mass, only the orbital angular momentum is immediately changed by the impulse. Furthermore, we assume that the pre-impact system is in an equilibrium configuration, and therefore the mutual orbit is circular. Thus, the impulse to the free angular momentum is equal to

$$\Delta H = \frac{m_A m_B}{m_A + m_B} r \Delta v. \quad (17)$$

Substituting our definition for  $\beta$  into this expression gives the free angular momentum perturbation as a function of  $\beta$ :

$$\Delta H = -\beta \nu m_{\text{DART}} v_{\text{DART}} r, \quad (18)$$

where again the negative sign is due to the retrograde impact. Finally, we add this perturbation to the equilibrium free angular momentum value for use in the equations of motion:

$$H_{\text{free}} = H^* + \Delta H. \quad (19)$$

Using this expression for the free angular momentum allows  $r$ ,  $\theta$ , and  $\lambda$  to oscillate around their equilibrium values, allowing for the exchange of momentum between the orbit and the secondary's spin.

## 3. Results

For the following results, we use a nominal configuration for the Didymos system where the initial separation distance  $r$  is 1.2 km, the secondary's bulk diameter is equal to 164 m, and the secondary's axis ratios are  $a/b = 1.3$  and  $b/c = 1.2$  (see Table 1). Here  $a$  is the semi-major axis of the ellipsoidal secondary,  $b$  is the semi-intermediate axis, and  $c$  is the semi-minor axis. The  $c$  axis corresponds to the maximum principal moment of inertia and spin axis of the secondary, while the  $a$  axis points toward the primary in equilibrium. In normalized units, the equilibrium free angular momentum for the nominal case is about 3.4, resulting in an equilibrium orbit period of about 11.92 hr, consistent with the value in Table 1. Using the equations of motion for the simplified system, we can choose a value of  $\beta$  to examine the behavior of the excited state.

### 3.1. Analytic Results

Assuming that the system is initially at equilibrium, we have all the initial conditions necessary to integrate the equations of motion. We simulate the impact by instantaneously perturbing the free angular momentum for a given value of  $\beta$ . When the free angular momentum is perturbed through  $\beta$ , the system deviates from the equilibrium configuration. The inertia tensor of the secondary is calculated using its bulk diameter and axis ratios, while the inertia tensor of the primary is calculated by approximating the primary's full shape model as an oblate spheroid. Thus, we have all the quantities needed to propagate the equations of motion.

We integrate Equations (11)–(13) forward in time for a nominal case where  $\beta = 3$  to solve for  $r$ ,  $\lambda$ , and  $\theta$ . Time histories of  $r$  and  $\lambda$  are shown in the top plots of Figure 2 for the full 50-day integration period, and a 3-day close-up of these results is shown in Figure 3.

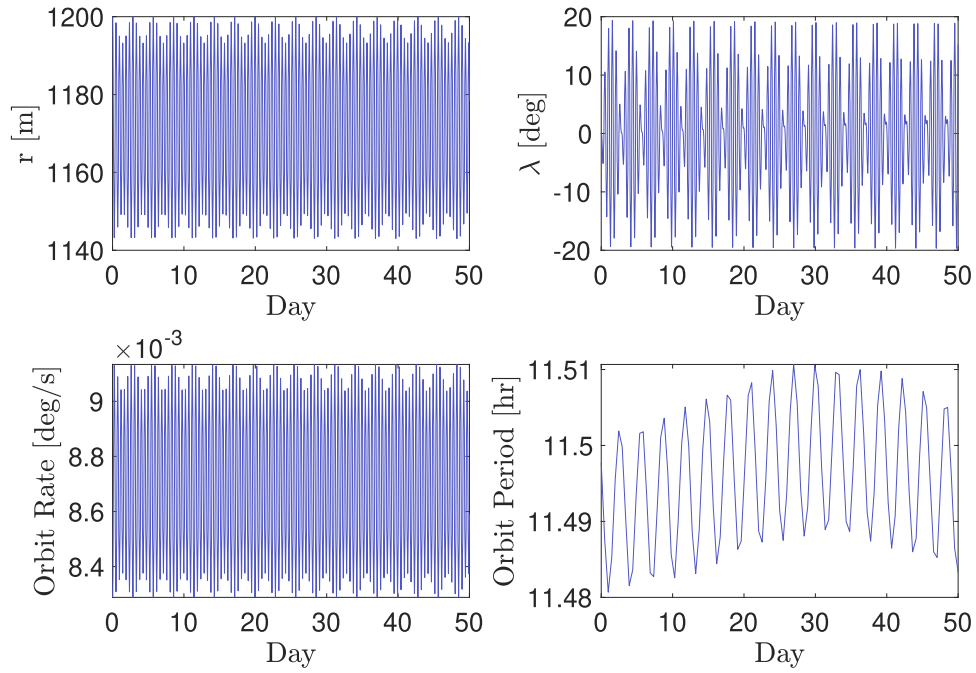


**Figure 2.** Separation (top left), libration (top right), orbital rate (bottom left), and orbital period (bottom right) for the case  $\beta = 3$  for a time of 50 days.

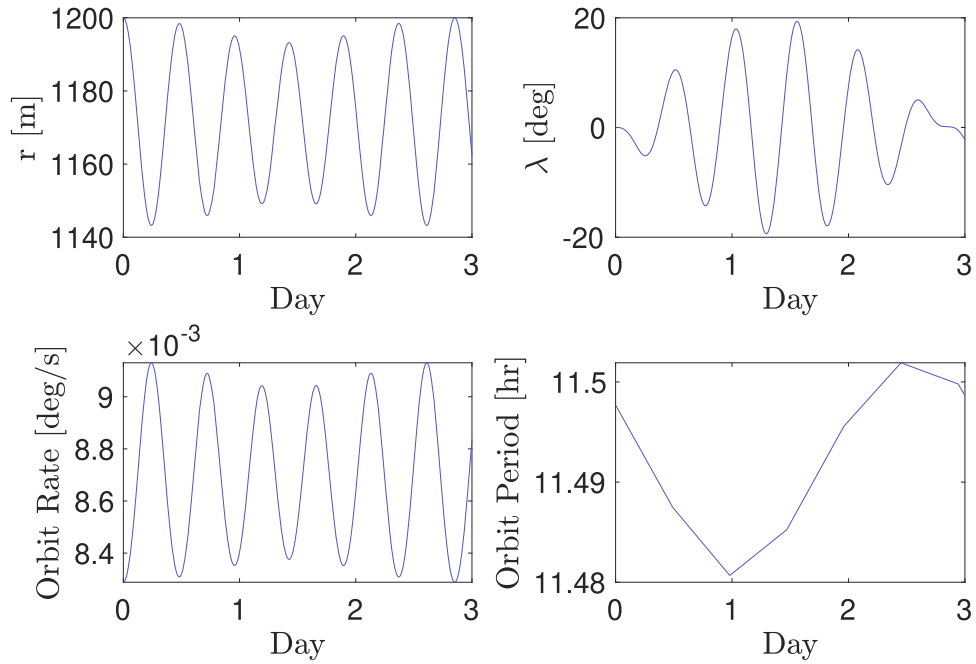


**Figure 3.** Close-up view of the separation (top left), libration (top right), orbital rate (bottom left), and orbital period (bottom right) for the case  $\beta = 3$  for a time of 3 days.

The libration amplitude is calculated using the time history of  $\lambda$  over the full time domain. A  $20^\circ$  libration means that the secondary is oscillating by  $\pm 20^\circ$  around the line  $r$ , as is the case in Figure 3.

The orbit rate  $\dot{\theta}$  is plotted for the  $\beta = 3$  case in the bottom left panel of Figures 2 and 3, where we immediately see that it varies over time. In order to calculate the orbit periods, we use an event function during the integration of the equations of motion. The event function checks the integration of Equation (11) and calculates the precise times  $\theta$  has reached  $2\pi$ . By differencing these sequential times, we calculate the

orbit period, or the time required for the mutual orbit to move by  $2\pi$  rad in inertial space. This is what an ideal light curve would see, and therefore it is the most accurate representation of real-world dynamics for our model.

Figures 2 and 3 show the result of this numeric integration approach, plotting the orbit period as a function of time in the bottom right panels. These results clearly show that the orbit period is not constant when the system is perturbed from its equilibrium. We calculate the orbit period variation simply by taking the elementary range of the orbit period over its time history, i.e., differencing the maximum and minimum values in

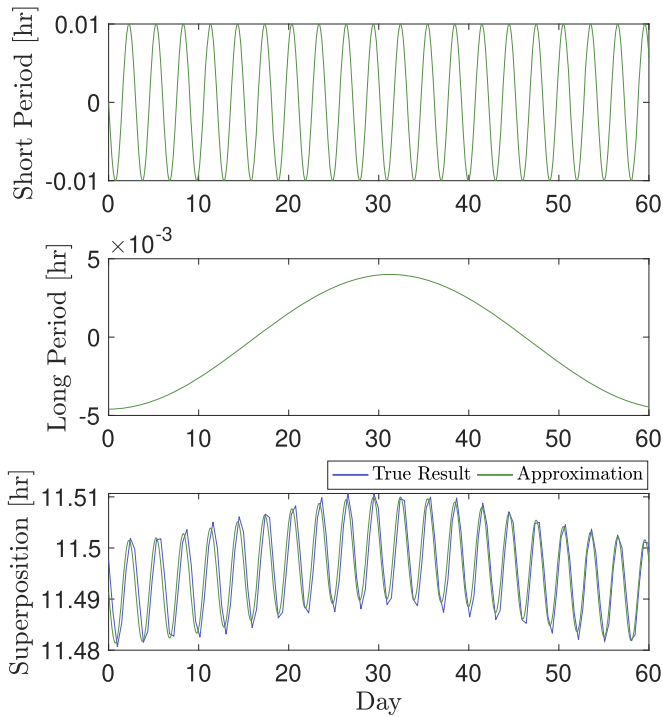


**Figure 4.** Decomposition of the orbit period variations into its two constituent modes. The decomposition is computed using a discrete Fourier transform. The short-period mode (top), long-period mode (middle), and superposition of the two modes (bottom) are plotted, with the superposition overlaid on the actual orbit period calculation.

the full time domain. Thus, for this nominal case shown in Figure 2, the orbit period variation is roughly 0.03 hr, or about 110 s. Further discussion on the relevancy of these variations to actual observations is in Section 6.

The two timescales between Figures 2 and 3 demonstrate the various modes that drive the dynamics. Estimating these frequencies using a discrete Fourier transform and analyzing the resulting power spectral density, the dynamics of the separation, libration, and orbit rate all have a short-period frequency roughly equal to the system’s mean motion, with a period around 12 hr. There is also a long-period mode with a period of about 3 days. The frequencies of these modes are dependent on the shape of the secondary and the value of  $\beta$  (Agrusa et al. 2021).

Separate from but related to the modes in  $r$ ,  $\lambda$ , and  $\theta$ , the orbit period fluctuations also appear to be driven by two modes: a short period and a long period. Again, we estimate these frequencies by taking a discrete Fourier transform of the time history and analyzing the power spectral density. Here, the short-period mode of the orbit period variations has a period of approximately 3 days, while the long-period mode for the orbit period variations has a period of around 60 days. The short-period mode has an amplitude of about 80 s, while the long-period mode has an amplitude of about 30 s, estimated from the power spectral density. Both of these modes are important, and the total period variation over time is the sum of these two amplitudes. These two modes are plotted in Figure 4, and their superposition is also compared to the actual orbit period calculation. Note that these modes are only representative and will change with different secondary shapes and values of  $\beta$ . A more in-depth discussion on the constituent modes is given in Section 4.5. Since we are mainly interested in the orbit period

variations, in the remainder of this work “short period” and “long period” will refer to the modes that drive the orbit period, and not those in the separation, libration, and orbit rate.

### 3.2. GUBAS Results

In order to propagate the full numeric GUBAS simulations, we use  $\beta$  to calculate the equivalent  $\Delta v$  to apply to the system through the relationship in Equation (18). The initial conditions are again chosen such that the system is in equilibrium. To achieve this, we choose a separation distance of 1200 m and a perpendicular velocity equal to the instantaneous circular orbit speed. However, this does not guarantee that the system will have the desired initial orbit period to match Didymos. We therefore iterate the density until the initial orbit period is equal to 11.92 hr, the observed orbit period of Didymos. This is also equal to the spin period of the secondary in the 1:1 spin-orbit resonance. After iteration, the system density is equal to about  $2.2 \text{ g cm}^{-3}$ , well within the uncertainty on Didymos’s density. This results in initial conditions that produce a nearly circular orbit with damped libration and a nearly constant orbit period, while keeping all characteristics of the system within the uncertainties listed in Table 1.

The full numeric simulations then start from the equilibrium initial conditions, with the exception of the velocity perturbation. The GUBAS results are used for validation of the analytic results, as well as a more accurate representation of the dynamics in Section 5. GUBAS uses full three-dimensional simulations with a coupled gravity potential truncated to fourth degree and order along with the full primary shape model to obtain the most accurate model of the Didymos system. We will compare our analytic results to three separate GUBAS simulations:  $\beta = 1, 2, \text{ and } 3$ .

In the GUBAS results, the secondary’s orientation is tracked using a set of 1–2–3 Euler angles (roll-pitch-yaw), where  $\theta_1$  (roll) measures rotation about the secondary’s long axis ( $x$ -axis), which initially points at the primary.  $\theta_2$  (pitch) measures rotation about the secondary’s intermediate axis ( $y$ -axis), and  $\theta_3$  (yaw) measures rotation about the secondary’s shortest axis ( $z$ -axis), which is initially aligned with the secondary’s spin pole perpendicular to the orbit plane. We are concerned with the planar libration, which is  $\theta_3$ , or yaw. Rotations in  $\theta_1$  and  $\theta_2$  are very small in this case and are consequently ignored. Attitude instabilities are possible depending on the size of the secondary and the value of  $\beta$ , in which case  $\theta_1$  and  $\theta_2$  are important (Agrusa et al. 2021). However, for now we only consider cases where the attitude remains stable. We measure the libration amplitude only using the time history of  $\theta_3$ .

Calculating the orbit period is slightly different: each time the secondary crosses a predefined inertial plane in the GUBAS results, the time of crossing is recorded. Generally, we simply define this plane to be the inertial  $y$ - $z$  plane. Each of these crossing times is then differenced to calculate the time between the plane passages, similar to the time between occultations in actual binary asteroid observations. This is analogous to our approach in the analytic case, where we are concerned with a physical interpretation of the orbit period. We calculate the variation in the orbit period again by differencing the maximum and minimum values of the orbit period over the full time domain.

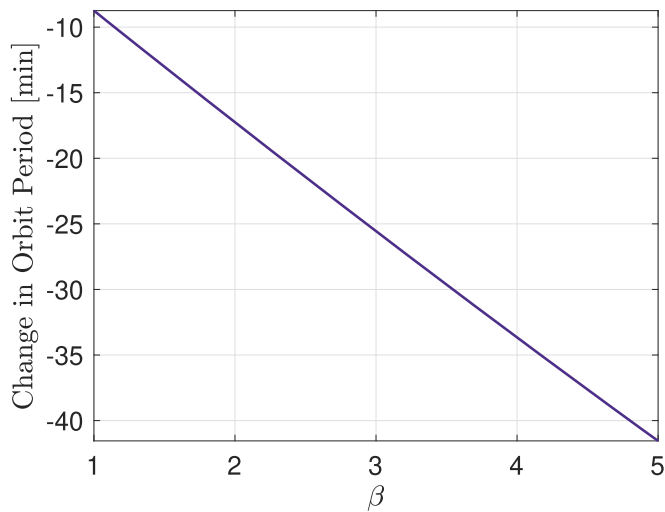


**Figure 5.** Change in mean orbit period as a function of the  $\beta$  parameter.

#### 4. Sweep over Momentum Enhancement Factor

In order to examine the system's response to the DART impact, we will sweep through multiple values of the momentum enhancement factor  $\beta$ . The minimum value of  $\beta$  is 1, and we increase this up to a value of  $\beta = 5$ . In this way we investigate how increasing the momentum transfer of the impact affects the resulting dynamics.

##### 4.1. Mean Orbit Period Change

By calculating the average orbit period following the impact, we can obtain a single mean orbit period ignoring the variations. We have already calculated the initial equilibrium orbit period, and by differencing these we can estimate the expected change in mean period for a value of  $\beta$ . We can test over multiple values of  $\beta$ , here ranging between 1 and 5, to plot the change in orbit period as a function of  $\beta$ . This is shown in Figure 5.

This is one of the expected DART results: a change in orbit period caused by the impact. This is the result that will be measurable from ground-based observations. A strongly linear relationship between  $\beta$  and the change in orbit period is evident, with a negative slope resulting from the retrograde impact. This shows that the minimum value of  $\beta = 1$  changes the orbit period by approximately 9 minutes, or about 1% of the equilibrium orbit period.

##### 4.2. Libration-induced Variations in Orbit Period

While DART will clearly change the mean orbit period, it will also cause the orbit period to fluctuate about the mean by inducing librations in the secondary. Using the analytic model, we test multiple values of  $\beta$  ranging between 1 and 5 and calculate the resulting libration amplitude and orbit period variations as detailed in Section 3.1. In addition, several GUBAS simulations are included for  $\beta$  values of 1, 2, and 3 for comparison and validation. The analytic and numeric results are all shown in Figure 6.

Figure 6 shows that even the smallest value of  $\beta = 1$  has fluctuations in its orbit period of about 40 s. That increases to more than a minute and a half at a  $\beta$  value of 3. Thus, even modest libration can result in significant variations in the orbit

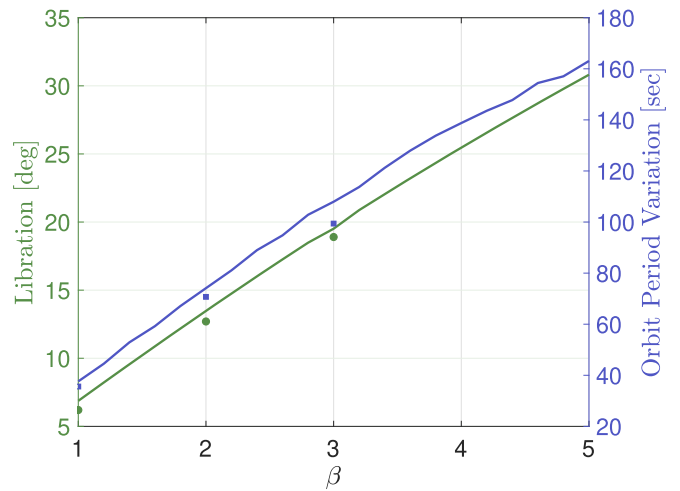


**Figure 6.** The libration and orbit period variations as functions of  $\beta$ . The left axis (green) indicates the libration amplitude, and the right axis (blue) shows the variation in the orbit period. The results from fully coupled GUBAS numeric simulations are overlaid as data points and agree well with the analytic model.

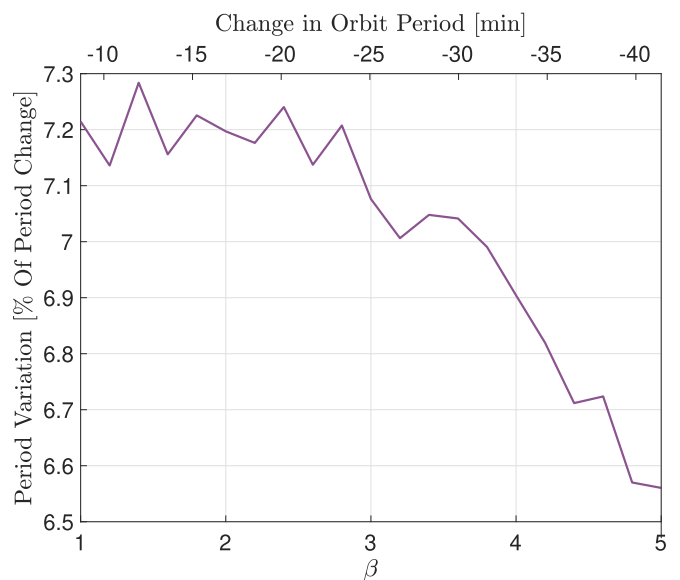


**Figure 7.** Variation in orbit period as a percent of the change in orbit period for varying values of  $\beta$ . The curve is also plotted against the actual change in orbit period.

period. These results agree well with selected GUBAS simulations, which are shown as data points in Figure 6.

Next, we calculate the orbit period variation as a percentage of the change in mean orbit period. This is plotted in Figure 7, showing that the smallest values of  $\beta$  have the largest relative variations compared to the impulsive change to the mean orbit period. For example, at  $\beta = 1$ , there is only about a 9-minute change to the mean orbit period, but the orbit period fluctuates by around 40 s, which is about 7% of 9 minutes. Compare this to  $\beta = 5$ , where the mean orbit period changes by more than 40 minutes but sees fluctuations on the order of 160 s, which is only about 6.5% of the period change.

##### 4.3. Effect of Axis Ratio

While up to now we have only focused on the nominal case  $a/b = 1.3$  and  $b/c = 1.2$ , it is worthwhile to investigate the effect of the axis ratios on the behavior of the system. While

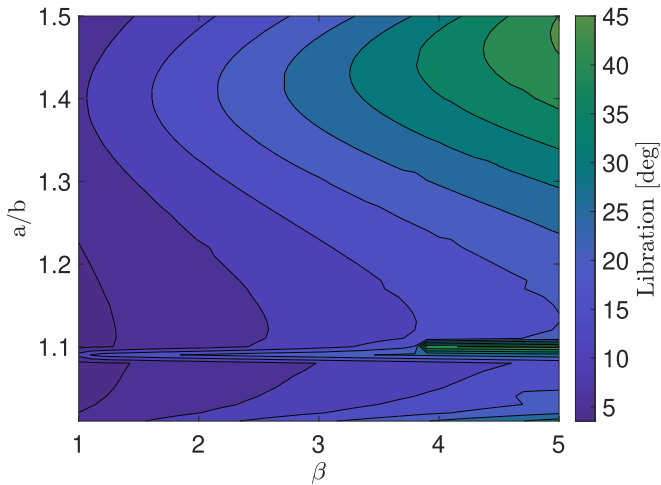


**Figure 8.** Libration amplitude as a function of the axis ratio  $a/b$  and the  $\beta$  parameter.

$b/c$  does not have a large effect on the secondary’s response owing to the planar dynamics,  $a/b$  does affect the dynamics significantly. Thus, we will test additional values of  $a/b$  while holding  $b/c$  constant. We allow  $a/b$  to vary between 1.0 and 1.5, the typical range of secondary axis ratios (Pravec et al. 2016), while still varying  $\beta$  between 1 and 5. Figure 8 shows the libration amplitude as a function of both  $a/b$  and  $\beta$ , while Figure 9 shows the corresponding variation in the orbit period.

Still immediately apparent is that increasing  $\beta$  increases both the libration amplitude and the orbit period variations. However, we also notice a strong dependence on  $a/b$ . For example, there is a resonance near  $a/b = 1.1$ , where the libration and orbit period variation are excited for all values of  $\beta$ . This is a 2:1 resonance between the libration frequency and mean motion, as discussed in Agrusa et al. (2021). The 1:1 resonance between these frequencies occurs near  $a/b = 1.4$ , which is visible in these plots but not as sharp as the resonance at  $a/b = 1.1$ .

As  $a/b$  changes, the moments of inertia of the secondary change as well. Also, the natural frequencies of oscillations in the secondary change with  $a/b$  (Agrusa et al. 2021). Thus, it is unsurprising that the libration magnitude changes with  $a/b$ . However, it is interesting that there is not a monotonic dependence on  $a/b$ . As an explanation, note that certain shapes excite resonances with the mean motion. While the 2:1 resonance at  $a/b = 1.1$  appears to be very narrow, the width of the 1:1 resonance near  $a/b = 1.4$  is much wider. This is consistent with the findings in Agrusa et al. (2021) and provides one explanation for the complicated relationship between the libration and  $a/b$ .

Lastly, Figure 10 shows the variations in the orbit period as a percent of the mean orbit period change. This is the same approach taken in Figure 7, so that Figure 7 is a single line in Figure 10. The mean period change does not depend on the axis ratio  $a/b$ . However, increasing  $a/b$  does increase the variation in the orbital period.

#### 4.4. Nonequilibrium Impact

Up to this point we have assumed Didymos to be in an equilibrium configuration prior to impact. In this state the secondary is perfectly tidally locked and the libration before impact has been damped to  $0^\circ$ . However, it is possible that

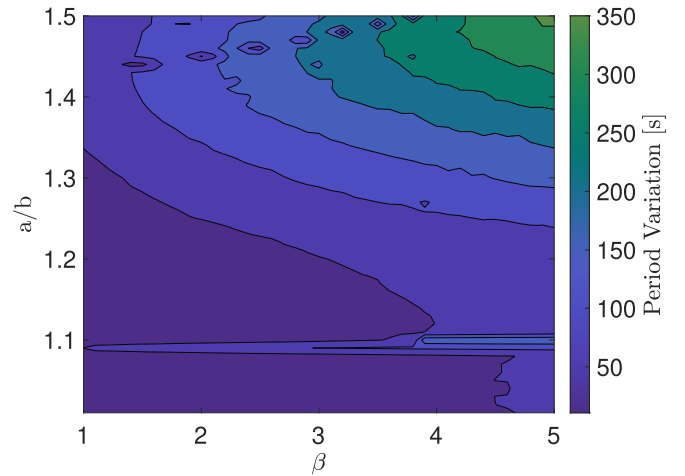


**Figure 9.** Variation in orbit period as a function of the axis ratio  $a/b$  and the  $\beta$  parameter.

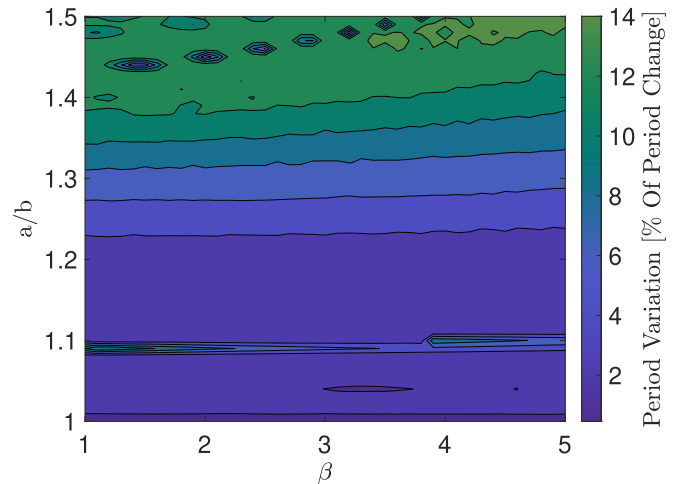


**Figure 10.** Variation in orbit period as a percentage of the mean period change for values of the axis ratio  $a/b$  and the  $\beta$  parameter.

Didymos is not exactly in an equilibrium state before the DART impact. We now examine the post-impact behavior for a system that was not previously in an equilibrium. We test four different excitation levels, perturbing the equilibrium free angular momentum by  $\pm 0.01$  and  $\pm 0.02$  in normalized units (corresponding to maximum libration amplitudes of  $5^\circ$  and  $10^\circ$ , respectively). Two of these cases have a free angular momentum higher than the equilibrium value, and the other two have one lower than the equilibrium value. At each of these levels of perturbation, we run two cases: one with the libration amplitude at the impact epoch equal to  $0^\circ$ , and the other with the libration amplitude at its maximum value for the excitation level, either  $5^\circ$  or  $10^\circ$ . Thus, we have eight perturbed test cases in addition to the equilibrium case. First, the overall average period change is shown in Figure 11. This demonstrates that the average period change is largely unaffected by impacting a nonequibrated system. However, systems with a free angular momentum higher than the equilibrium see slightly larger changes in their orbit period, whereas systems below the equilibrium free angular momentum see slightly smaller changes. The effect is more pronounced farther away from the equilibrium. The orientation of the secondary at impact has

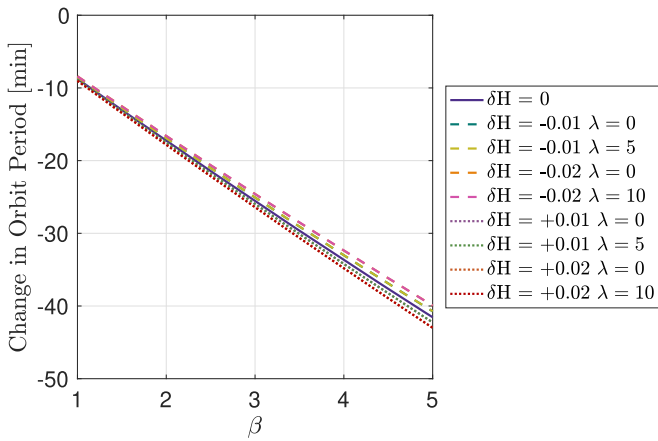


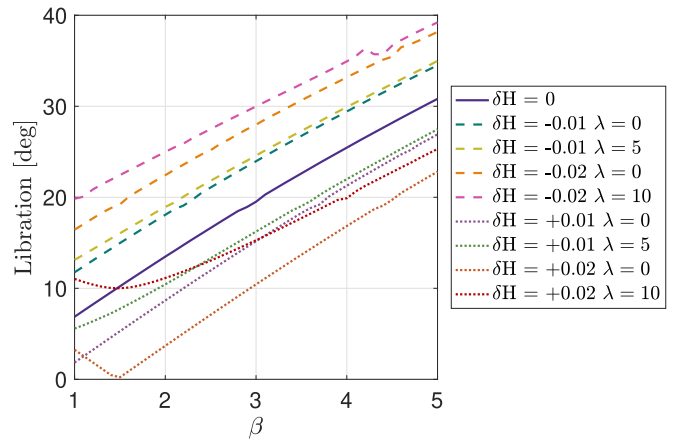
**Figure 11.** Overall average period change as a function of  $\beta$  for the initial equilibrium and several perturbed cases.

no bearing on the mean period change, regardless of the level of system excitation.

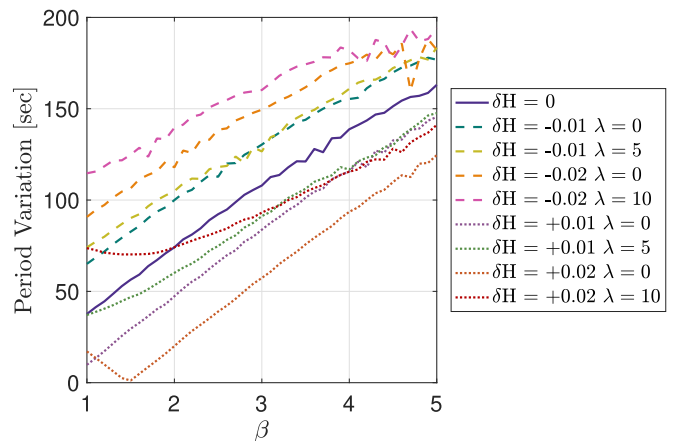
Figure 12 shows the libration amplitude as a function of  $\beta$  for all test cases. We see clear differences between the cases above the equilibrium and cases below the equilibrium. In general, systems with an initial configuration below the equilibrium angular momentum have larger resulting libration amplitudes following the impact. This is expected, since the impact will move the system farther from equilibrium. Additionally, impacts when the secondary is at its apex of libration see a more energetic response than impacts at  $0^\circ$  libration. Systems with an initial angular momentum larger than the equilibrium value see a more diverse range of responses. For systems only slightly perturbed above the equilibrium, even the smallest impact is enough to decrease the angular momentum back through the equilibrium value to a value below it. For systems that are initially more excited, we see that increasing the impact momentum transfer pushes the system back toward equilibrium and the libration amplitude begins to decrease as  $\beta$  increases. However, once  $\beta$  is large enough to push the system back below equilibrium, the libration amplitude then begins to increase as  $\beta$  increases. Again, we see a more energetic response when the impact occurs at the secondary’s libration apex than when the impact occurs at  $0^\circ$  libration.

Figure 13 shows the variation in orbit period as a function of  $\beta$  for the same test cases. Here we see very similar behavior to the libration amplitude response. Systems initially below the equilibrium angular momentum are pushed farther away from equilibrium, whereas systems above the angular momentum are first pushed back toward equilibrium and then further below it as  $\beta$  increases. This further reinforces the idea that the libration amplitude and orbit period variations have nearly the same trend as a function of  $\beta$ .

Another concern for an initially nonequilibrium system is out-of-plane motion, where the secondary rocks about its long axis, as this can be long-lived in binary asteroids (Quillen et al. 2021). This out-of-plane rotation would also cause the system to be initially perturbed from the equilibrium value of angular momentum. However, the perturbation is small since the out-of-plane rotations are about the minimum principal inertia axis; the secondary’s angular momentum is still dominated by its rotation about the maximum principal inertia axis. Therefore, the system is not far from equilibrium. Furthermore, the excess



**Figure 12.** Libration amplitude as a function of  $\beta$  for the initial equilibrium and several perturbed cases.



**Figure 13.** Variation in orbit period as a function of  $\beta$  for the initial equilibrium and several perturbed cases.

angular momentum goes into the out-of-plane rotation instead of in-plane libration. Therefore, we expect the post-impact libration in this scenario to be similar to the planar case, i.e., relatively unaffected by the initial out-of-plane rotation. So we do not expect initial out-of-plane rotations to have a significant effect on the dynamics, at least for small values of  $\beta$ . A more important consequence of initial out-of-plane rotation is that it becomes easier for the impact to further excite this rotation mode, known as the barrel instability (Ćuk et al. 2021), and the secondary may start tumbling at lower values of  $\beta$  than expected otherwise.

#### 4.5. Constituent Modes of Variations

As shown in Section 3.1, the orbit period variations are driven by two modes: a short period and a long period. However, the constituent modes are affected by both  $a/b$  and  $\beta$ . An example of this is shown in Figure 14, where the instantaneous orbit period is plotted over time for  $a/b$  varying between 1.1 and 1.5, all for  $\beta=3$ . Each axis ratio shows a unique behavior in the orbit period, highlighting the strong dependence on the secondary’s shape.

To compare the behavior of the orbit period variations, we compute the discrete Fourier transform of each time history and compare their power spectral densities to obtain estimates of the period and amplitude of the constituent modes. The Fourier transform struggles to obtain accurate values of the frequencies

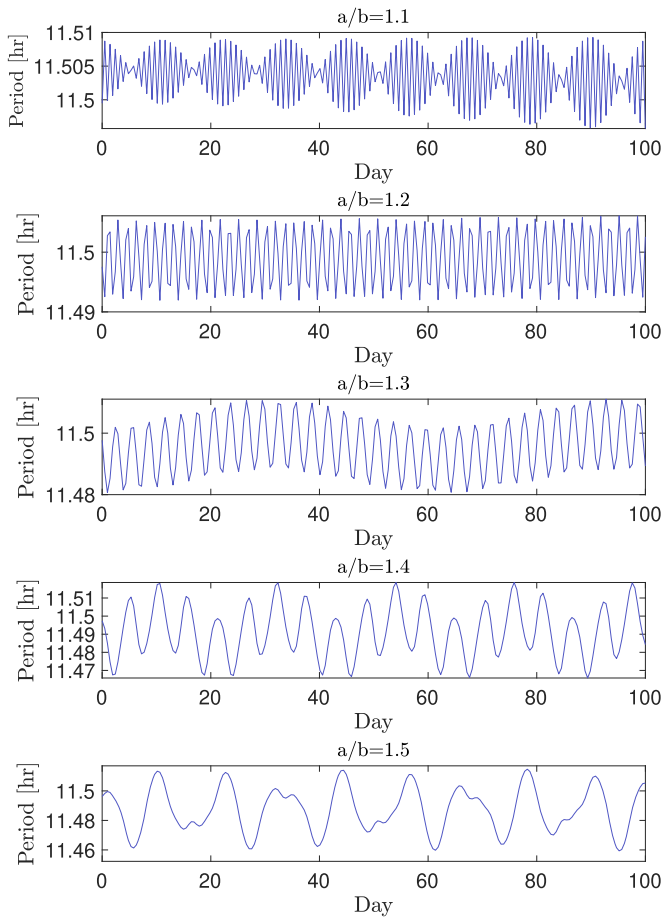


**Figure 14.** The instantaneous orbit period for different values of  $a/b$ , all for  $\beta = 3$ . The orbit period variation behavior strongly depends on  $a/b$ .

owing to the discretization of the orbit period. Since only one data point is obtained per orbit period, the sampling frequency is necessarily coarse. To counteract this, we use a long time domain of 500 days. However, the results are only estimates of the true behavior owing to this shortcoming.

Table 2 shows the results of the Fourier transform. The period and amplitude estimates of the short- and long-period modes are reported for values of  $a/b$ . Note that the transform did not find a long-period mode for  $a/b = 1.2$ . Additionally, a third mode for  $a/b = 1.1$  causes beating, with a period of approximately 11 days. Recall the resonance at  $a/b = 1.1$ , which may explain this unique behavior in the orbit period variations. In general, Table 2 suggests that increasing  $a/b$  will increase the short period. The short-period amplitude also increases with  $a/b$  until after  $a/b = 1.4$ , where it suddenly decreases. Note the inclusion of  $a/b = 1.25$ , which is approximately the longest mode with nonnegligible amplitude. The DART mission must measure the post-impact period to an accuracy of 7.3 s (Cheng et al. 2018), so observations must span the length of any long-period mode with amplitude larger than  $2 \times 7.3 = 14.6$  s. For  $\beta = 3$ , any long-period mode for  $a/b = 1.24$  or less has an amplitude below this threshold. The long-period mode amplitude has its minimum at  $a/b = 1.2$ , where it is nonexistent, and then increases in both directions as  $a/b$  changes. The period behaves oppositely, where it can be thought of as infinitely long at  $a/b = 1.2$  and decreases as  $a/b$  changes in either direction. In this way, any  $a/b$  close to 1.2

**Table 2**

The Period and Amplitude of the Short- and Long-period Constituent Modes of the Orbit Period Variations for Values of  $a/b$ , All Using  $\beta = 3$

$a/b$	Short-period Mode		Long-period Mode	
	Period	Amplitude	Period	Amplitude
1.1	1 day	48.4 s	250 days	8.6 s
1.2	1.7 days	63.0 s	N/A	N/A
1.25	2.2 days	63.4 s	125 days	19.2 s
1.3	3.0 days	83.9 s	62.0 days	31.1 s
1.4	5.4 days	127.3 s	21.8 days	70.7 s
1.5	6.8 days	68.0 s	11.4 days	136 s

**Note.** These estimates are obtained through a discrete Fourier transform of the instantaneous orbit period time histories.

**Table 3**

The Period and Amplitude of the Short- and Long-period Constituent Modes of the Orbit Period Variations for Values of  $\beta$ , All Using  $a/b = 1.3$

$\beta$	Short-period Mode		Long-period Mode	
	Period	Amplitude	Period	Amplitude
1	3.4 days	32.4 s	54 days	14.3 s
2	3.2 days	56.7 s	58 days	26.9 s
3	3.0 days	84.7 s	62 days	30.8 s
4	2.8 days	103.7 s	70 days	37.0 s
5	2.6 days	130.9 s	88 days	40.1 s

**Note.** These estimates are obtained through a discrete Fourier transform of the instantaneous orbit period time histories.

will have a very small long-period mode amplitude with a very long period.

Next, we repeat the same process but holding  $a/b = 1.3$  constant and varying  $\beta$  from 1 to 5. The estimates for the amplitudes and periods of the modes are shown in Table 3. As expected, increasing  $\beta$  increases the amplitudes of both the short- and long-period modes. The results also suggest that increasing  $\beta$  decreases the short period, while the long period increases.

The short- and long-period modes appear to be driven by the apsidal precession of the eccentricity vector, which is measured by the longitude of periapsis. On average, the longitude of periapsis precesses with a frequency equal to the long-period mode in the orbit period variations. Within that precession, the eccentricity vector also sees short-period oscillations, with a period equal to the short-period mode in the orbit period variations. Interestingly, the eccentricity *magnitude* oscillates at the same frequency as the separation and libration, which is not the same as the short-period mode in the orbit period variations. Instead, the orbit period variations are driven by the *orientation* of the eccentricity vector as the elliptical orbit precesses.

While this provides a physical interpretation of the frequencies, it is desirable to obtain an analytic approximation of the frequencies that drive the orbit period variations. To accomplish this, we compute an equilibrium solution at the new value of free angular momentum,  $H_{\text{free}}^*$ , giving us an equilibrium separation  $r^*$  and orbital frequency  $n^*$ . We then treat the post-impact system as a perturbed solution around this new equilibrium and compute the corresponding linearized solution. The variations in  $r$  and  $\lambda$  can be expressed as

$$\delta r(t) = A_r \cos \omega_1 t + B_r \cos \omega_2 t \quad (20)$$

$$\delta\lambda(t) = A_\lambda \cos \omega_1 t + B_\lambda \cos \omega_2 t, \quad (21)$$

where the coefficients  $A_i$  and  $B_i$  are constants that depend on the system parameters. However, we are mostly concerned with the frequencies, so we focus on  $\omega_1$  and  $\omega_2$ , which are the linearized frequencies driving oscillations in  $r$  and  $\lambda$ . These frequencies can be found as the solution of the biquadratic equation:

$$\xi^4 + \alpha\xi^2 + \gamma = 0, \quad (22)$$

with

$$\alpha = \frac{3\mathcal{G}(m_A + m_B)(m_B(I_s - I_{1z}) + m_A(I_{2y} - I_{2z}))}{2m_A m_B r^{*2}} + \frac{\mathcal{G}(m_A(-3I_{2x} + 3I_{2y} + I_{2z}) + m_B I_{2z})}{I_{2z} r^{*3}} \quad (23)$$

and

$$\begin{aligned} \gamma = & \frac{-3\mathcal{G}^2(I_{2x} - I_{2y})(m_A + m_B)}{2I_{2z} m_A m_B^2 r^{*10}} \\ & \times (-3m_A m_B r^{*2}(m_B(I_{1z} + 2I_{2z} - I_s) \\ & + m_A(-2I_{2x} + I_{2y} + 3I_{2z})) \\ & - 15I_{2z}(m_A + m_B)(m_B(I_{1z} - I_s) \\ & + m_A(-2I_{2x} + I_{2y} + I_{2z})) + 2m_A^2 m_B^2 r^{*4}). \end{aligned} \quad (24)$$

The derivation of these coefficients is outlined in the [Appendix](#). We now turn to the orbit period, and we approximate the orbital displacement as

$$\theta(t) = n^* t + A_1 \cos \omega_1 t + A_2 \cos \omega_2 t. \quad (25)$$

Expressing time as  $t = pT_0 + \delta T$ , where  $T_0 = 2\pi(n^*)^{-1}$  and  $\delta T$  is the variable deviation from this value, we obtain an approximate expression for  $\theta(t)$  ignoring second-order terms:

$$\theta(t) = 2p\pi + A_1 \cos \frac{2p\pi\omega_1}{n^*} + A_2 \cos \frac{2p\pi\omega_2}{n^*} + \delta T n^*, \quad (26)$$

where  $p$  is an integer number of orbits. Setting the approximate  $\theta(t) = 2p\pi$  allows us to compute the correction  $\delta T$  after  $p$  orbits:

$$\delta T(p) \approx \frac{A_1 \cos \frac{2p\pi\omega_1}{n^*} + A_2 \cos \frac{2p\pi\omega_2}{n^*}}{-n^*}. \quad (27)$$

A Fourier analysis of this approximation shows that the dominant frequencies driving the orbit period variations are approximately  $(n^* - \omega_1)$  and  $(n^* - \omega_2)$ . Owing to the linearization, this approximation is only accurate at small values of  $\beta$  and becomes less accurate as  $\beta$  increases. However, it provides a good first approximation of the frequencies that drive the orbit period variations. For example, for the axis ratio  $a/b = 1.3$ , at  $\beta = 1$  this method calculates the short period equal to 3.4 days and the long period equal to 50 days. This is more accurate than the  $\beta = 3$  estimate, which calculates the short period equal to 3.3 days and the long period equal to 48 days. Note that the short-period mode remains relatively accurate at larger  $\beta$ , but the long-period mode has the incorrect dependence on  $\beta$ . Nevertheless, this approach provides an analytic approximation of the frequencies of orbit period variations. This also reveals that the long-period mode, which is driven by the precession of the elliptical orbit, is strongly affected by nonlinear effects.

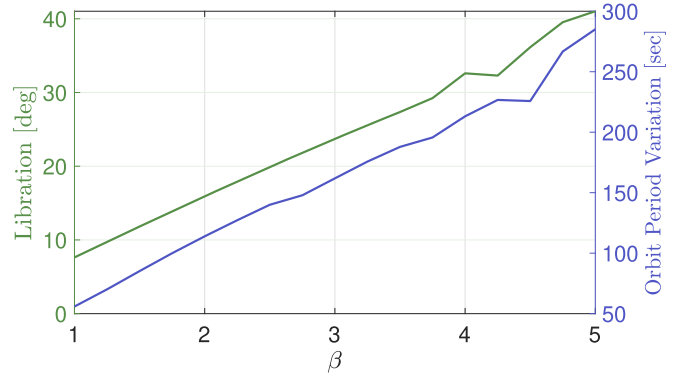


**Figure 15.** Libration and orbit period variation of the full 3D GUBAS simulations using a stand-in polyhedron model for Dimorphos.

## 5. High-fidelity Simulations

Up to now we have relied on the simplified model of McMahon & Scheeres (2013) to simulate the system dynamics, with only a few comparisons to high-fidelity simulations to validate our results. We now turn to GUBAS to run high-fidelity simulations, using full three-dimensional dynamics and polyhedron shape models for Didymos and Dimorphos. While a shape model exists for Didymos, there is none for Dimorphos. In this section we aim to avoid the ellipsoidal assumption on Dimorphos, since in reality it is unlikely to be symmetric and we wish to test the effect of an asymmetric secondary. We therefore use the shape model of Squannit, the secondary in the Moshup binary asteroid system, scaled to the expected size of Dimorphos. We adjust the shape model such that its volume is equivalent to the expected size of Dimorphos and its axis ratios are approximately  $a/b = 1.3$  and  $b/c = 1.2$ .

We use a more realistic three-dimensional impact geometry, where the  $\Delta v$  from the DART impact is applied at a vector approximately  $10^\circ$  “up” out of plane and  $10^\circ$  “out” in the radial direction. We again test values of  $\beta$  ranging from 1 to 5. Figure 15 shows the resulting libration and orbit period variation magnitudes for each simulation. Note that while the libration magnitudes are slightly larger than the simplified cases, the orbit period sees much larger variations. This demonstrates how the out-of-plane dynamics are important, as well as the coupled dynamics between more complicated shape models. These results also highlight the importance of obtaining an accurate estimate of Dimorphos’s shape and mass to model its dynamics.

Time histories of the orbit period for the  $\beta = 1, 3$ , and 5 simulations are plotted in Figure 16. Here we see that the two-mode structure appears in the  $\beta = 1$  and 3 cases, but not for  $\beta = 5$ . At  $\beta = 5$ , the impact transfers enough momentum to excite the barrel instability. This more complex rotation destroys the two-mode structure we saw in the planar cases. Again this illustrates the importance of considering the out-of-plane dynamics. However, this also shows that the simplified planar model is a fairly good prediction of the dynamics at low values of  $\beta$ .

## 6. Observation Implications

Due to the coupled relationship between the libration amplitude and the fluctuations in the orbit period, if one of these characteristics can be measured, it can offer insight into the other, provided that an estimate of the secondary’s shape

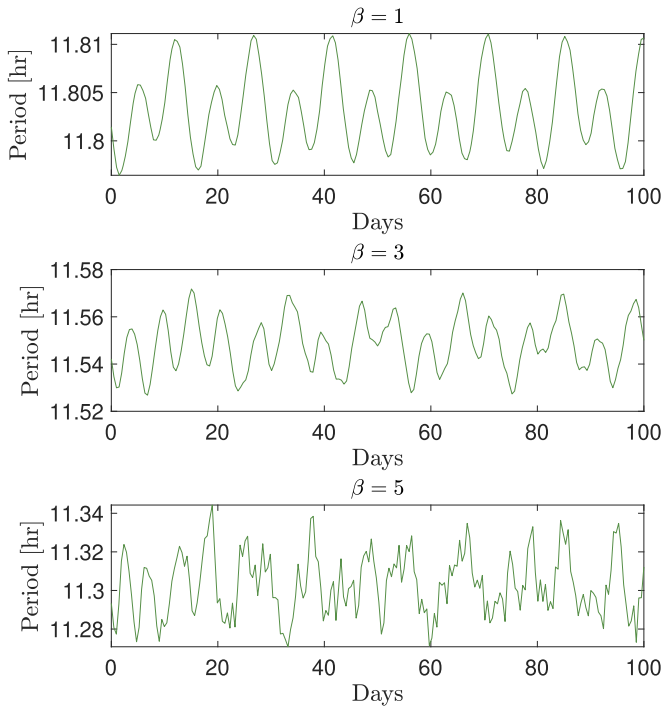


**Figure 16.** Time history of the orbit period for  $\beta = 1, 3,$  and  $5$  from the full 3D GUBAS simulations. At  $\beta = 5$  the two-mode structure breaks down and the orbit period variations become irregular. This corresponds to out-of-plane rotation in the barrel instability.

and mass is available. One possible application of this is constraining the libration state of the secondary through observations of the orbit period. Since the orbit period is easier to measure from the ground than the libration state, there is great potential in this approach. However, capturing the orbit period variations to sufficient accuracy may be difficult.

More relevant to the DART mission, however, is measuring the mean post-impact orbit period. To explore this process, we turn to the nominal case,  $a/b = 1.3$ ,  $b/c = 1.2$ , and  $\beta = 3$ . This is the case plotted in Figures 2 and 3. As discussed in depth, the orbit period fluctuations are driven by two frequencies: a short period and a long period. The short-period frequency has a period of about 3 days, while the long-period frequency has a period on the order of a few months. To capture the full orbit period variation, both these modes must be accounted for, as both of their amplitudes contribute to the overall variations in the orbit period.

### 6.1. Photometric Observations

To examine the modulation of the mean anomaly for photometric observation purposes, we model the instantaneous mean motion as a sum of two modes:

$$n(t) = \bar{n} + A_1 \cos(\omega_1 t - \phi_1) + A_2 \cos(\omega_2 t - \phi_2). \quad (28)$$

The average mean motion is about  $\bar{n} = 1.518 \times 10^{-4} \text{ rad s}^{-1}$ . The short-period mode has amplitude about  $A_1 = 1.458 \times 10^{-7} \text{ rad s}^{-1}$  and frequency about  $\omega_1 = 2.408 \times 10^{-5} \text{ rad s}^{-1}$ . The long-period mode has amplitude about  $A_2 = 5.556 \times 10^{-8} \text{ rad s}^{-1}$  and frequency about  $\omega_2 = 1.212 \times 10^{-6} \text{ rad s}^{-1}$ . The approximation is plotted with the actual mean motion variation in Figure 17, showing a close match.

This gives a mean anomaly modulation amplitude of the short period equal to  $A_1/\omega_1 = 0.35 \text{ deg}$  and long-period

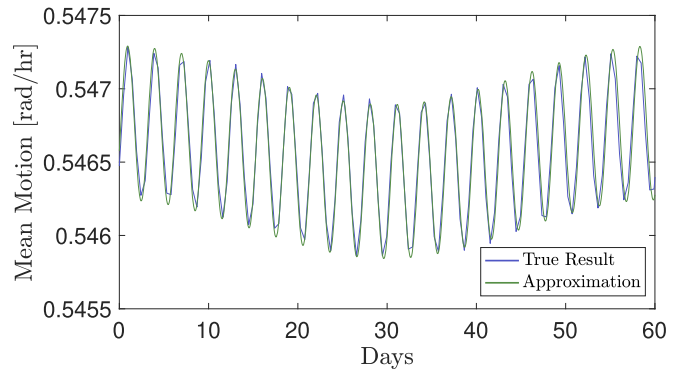


**Figure 17.** Instantaneous mean motion with the analytic approximation.

modulation amplitude equal to  $A_2/\omega_2 = 2.63 \text{ deg}$ . Since the short-period modulation of the mean anomaly is smaller than uncertainties in the event timings from other sources, mainly noise in the photometry measurements and irregularities in the asteroid shapes, it is negligible and can be considered as simply an additional source of noise. However, the long-period modulation is comparable to the event timing uncertainties from other sources and so must be considered. It is therefore necessary to spread observations over a few months to capture the long-period variation and ensure an accurate estimate of the mean orbit period.

### 6.2. Radar Observations

Radar observations of Didymos are planned at Goldstone and Green Bank starting in late 2022 September and lasting for up to 3 weeks. If the observations are bistatic, as planned, then the signal-to-noise ratios in 2022 will be about half as strong as they were during monostatic Goldstone observations in 2003, and as a result, the finest range resolution will probably be 75 m per pixel. This will show the positions of the primary and secondary at different epochs and will be sufficient to spatially resolve the primary but will place only a few pixels on the secondary owing to its relatively small size.

Due to the weak radar signal-to-noise ratios expected in 2022, it is very unlikely that the delay-Doppler images will have sufficient spatial resolution to reveal subtle variations in the orientation of the secondary at different epochs other than due to its orbital position. Librations will probably not be visible in the radar data.

It seems likely that the DART impact will cause variations superimposed on the impulsive change to the orbit period. The average change could become visible in the positions of Dimorphos within 1 week and possibly even more rapidly. The magnitudes of the short-period semimajor-axis variations are expected to be roughly 60 m, which is comparable to the finest range resolution provided by the radar observations. As such, it seems unlikely that variations with these periods will be evident in the radar imaging data, and at best, perhaps a periodic variation of 3 days *might* be visible in the residuals to orbital fits. The radar observations might span about 3 weeks, so it seems even less likely that the long-period mode will be visible. However, the uncertainties are considerable, so the data will be checked thoroughly just in case.

The variations in the orbit period are challenging in the context of the DART mission. One of the main requirements of the DART mission is to measure the change in orbit period to a precision of 7.3 s (Cheng et al. 2018). If the orbit period is

changing over time, it may be more difficult to meet this level of precision than originally thought owing to the additional noise on the mean orbit period generated by the variations. However, measuring the mean orbit period to within the required precision is possible despite the variations. Furthermore, provided that the libration is not damped over the 4 yr it will take for the arrival of Hera at Didymos, Hera may be able to directly measure the orbit period variations.

## 7. Discussion and Conclusion

The libration of the secondary is not independent of the mutual orbit dynamics in a binary asteroid system. Due to the conservation of angular momentum, fluctuations in the secondary's spin state cause a response in the orbital angular momentum. As a result, the orbital period is nonconstant in a librating binary asteroid system. If a system is in equilibrium with no libration, the orbit period is constant, but any deviations from that equilibrium will result in variations in the orbit period. There is a real-world example of a changing orbit period in binary asteroids. Variations appear in 1991 VH, where there is likely an interaction between the secondary's spin state and the orbit dynamics (Meyer et al. 2021; Pravec et al. 2021).

We see that the orbit period variations are driven by two modes, both of which have a significant amplitude. The variations are strongly dependent on  $\beta$  and the secondary axis ratio  $a/b$ , with certain values of  $a/b$  causing resonances in the dynamics. These modes are driven by the precession of the elliptical orbit and the orientation of the eccentricity vector.

The orbit period variations have significant implications for the observation of Didymos following the impact. It is unlikely that the short-period mode in the variations will be observable from the ground, but the long-period mode may need to be accounted for in observations. This offers an additional challenge for the DART mission, where measuring the post-impact orbit period may be more difficult owing to the variations. Note that this challenge will benefit from the complementarity of the Hera mission that will measure the post-impact state in great detail in the rendezvous with the target 4 yr later. Despite the difficulties provided by the orbit period variations, the mean orbit period change will still be measurable to the required accuracy.

If the secondary's shape is also known along with the initial system configuration and orientation at impact, the post-impact dynamics can provide an additional constraint on the estimation of  $\beta$  instead of relying solely on the mean period change. Thus, while orbit period variations are certainly a challenge in measuring the period, they can also provide an opportunity to gain more information on the impact. And since the orbit period variations are closely tied to the secondary's libration, they can also help constrain the libration state given proper knowledge of the secondary's shape and mass. This provides additional motivation for LICIAcube to accurately image the system just before the DART impact.

Agrusa et al. (2021) show that equilibrium configurations of Dimorphos are extremely sensitive to shape changes. If Dimorphos is a rubble-pile asteroid, its shape might be subject to small changes and medium-term adjustments, especially after the DART impact. In this case, the characteristic time of the shape change will be comparable to the orbital and spin period of Dimorphos. This is confirmed by preliminary results of rubble-pile simulations run using DEM codes PKDGRAV (Richardson et al. 2000) and GRAINS (Ferrari et al. 2017), which show that even small shape change can lead to

strong oscillations in Dimorphos's libration motion. Compared to the rigid-body case, the slow but steady deformation of the body facilitates the motion between stable and unstable regions identified by Agrusa et al. (2021). As discussed, in a binary system libration motion is closely connected to the orbital motion of the secondary, meaning that stronger libration oscillations reflect in larger fluctuations in the orbit period as well. A more detailed discussion of the rubble-pile case is provided in a dedicated paper, currently in preparation.

Most of this work assumed a planar impact through the secondary's center of mass. In reality, the impact will not be planar, as DART will impact Dimorphos at an angle of about  $10^\circ$  from the orbit plane (Cheng et al. 2018). Furthermore, it is likely that the actual impact will not be coincident with the center of mass in reality. Due to these simplifications, the analysis in this study likely does not capture all of the relevant dynamics, and the actual results are likely to be more complicated than predicted here. While Section 5 relaxed these assumptions for a more accurate analysis, it is by no means comprehensive. These simplifications were made to demonstrate the coupling between libration and orbit period variations, but the full nonplanar dynamics should be considered in future analysis of the impact, along with the torque imparted by the spacecraft on Dimorphos. An off-center impact will likely induce a higher libration magnitude, resulting in larger variations in the orbit period. The in situ dynamical and physical characterization of the target by Hera will allow us to ultimately remove the possible ambiguities in the impact.

We would like to thank the entire DART investigation team for helpful discussion throughout this study's development and preparation. This study was supported in part by the DART mission, NASA contract No. NNN06AA01C to JHU/APL. The work of P.P. was supported by the Grant Agency of the Czech Republic, Grant 20-04431S. P.M. acknowledges support from CNES and ESA. I.G., M.G., K.T., and P.M. acknowledge funding from the European Union's Horizon 2020 research and innovation program under grant agreement No. 870377 (project NEO-MAPP).

## Appendix

To derive the analytic approximations of the linear frequencies, we begin with the Hamiltonian of the planar model:

$$\mathcal{H} = \frac{1}{2} \left( \frac{p_\lambda}{I_{Bz}} + \frac{(p_\theta - p_\lambda)^2}{r^2 \mu} + \frac{p_r^2}{\mu} \right) + V(r, \lambda), \quad (\text{A1})$$

where the unnormalized potential is

$$\begin{aligned} V(r, \lambda) = & -\frac{\mathcal{G}m_A m_B}{r} - \frac{\mathcal{G}m_B}{2r^3} (2I_s + I_{Az}) \\ & - \frac{\mathcal{G}m_A}{2r^3} (I_{Bx} + I_{By} + I_{Bz}) + \frac{3\mathcal{G}m_B}{2r^3} I_s \\ & + \frac{3\mathcal{G}m_A}{4r^3} (I_{Bx} + I_{By} - (I_{By} - I_{Bx}) \cos 2\lambda). \end{aligned} \quad (\text{A2})$$

This leads to the equations of motion:

$$\dot{r} = \frac{\partial \mathcal{H}}{\partial p_r}, \quad \dot{p}_r = -\frac{\partial \mathcal{H}}{\partial r}, \quad \dot{\lambda} = \frac{\partial \mathcal{H}}{\partial p_\lambda}, \quad \dot{p}_\lambda = -\frac{\partial \mathcal{H}}{\partial \lambda}, \quad (\text{A3})$$

where

$$p_r = \frac{\partial \mathcal{L}}{\partial \dot{r}}, \quad p_\lambda = \frac{\partial \mathcal{L}}{\partial \dot{\lambda}}, \quad (\text{A4})$$

and  $\mathcal{L}$  is the Lagrangian of the planar system. From McMahon & Scheeres (2013), the binary is in an equilibrium configuration when

$$n^* = \sqrt{\frac{\mu}{r^{*3}} \left( 1 + \frac{3}{2r^{*2}} \left( \frac{I_{Az} - I_s}{m_A} + \frac{I_{By} + I_{Bz} - 2I_{Bx}}{m_B} \right) \right)}, \quad (\text{A5})$$

which also means

$$\lambda = \dot{\lambda} = 0. \quad (\text{A6})$$

Following the DART impact, we calculate the new angular momentum and the new equilibrium  $r^*$  and  $n^*$  that correspond to this angular momentum. We treat the initial condition (at impact) as a perturbed solution around the new equilibrium and compute the corresponding linearized solution. We introduce a deviation vector

$$\mathbf{w} = [\delta r, \delta \lambda, \delta p_r, \delta p_\lambda] \quad (\text{A7})$$

and the linearized system

$$\dot{\mathbf{w}} = \mathcal{J}\mathbf{w}, \quad (\text{A8})$$

where  $\mathcal{J}$  is the Jacobian of the flow Equations (A3). Substituting the new equilibrium condition ( $r^*$ ,  $n^*$ ) into Equation (A8), we obtain the characteristic polynomial

$$\xi^4 + \alpha \xi^2 + \gamma = 0; \quad (\text{A9})$$

here the coefficients  $\alpha$  and  $\gamma$  are as defined in Equations (23) and (24). The linearized frequencies  $\omega_1$  and  $\omega_2$  are then given as the solutions of the characteristic polynomial.

### ORCID iDs

Alex J. Meyer  <https://orcid.org/0000-0001-8437-1076>  
 Ioannis Gkolias  <https://orcid.org/0000-0003-4432-9863>  
 Harrison F. Agrusa  <https://orcid.org/0000-0002-3544-298X>  
 Daniel J. Scheeres  <https://orcid.org/0000-0003-0558-3842>  
 Kleomenis Tsiganis  <https://orcid.org/0000-0003-3334-6190>  
 Petr Pravec  <https://orcid.org/0000-0001-8434-9776>  
 Patrick Michel  <https://orcid.org/0000-0002-0884-1993>

### References

Agrusa, H. F., Gkolias, I., Tsiganis, K., et al. 2021, *Icar*, 370, 114624  
 Agrusa, H. F., Richardson, D. C., Davis, A. B., et al. 2020, *Icar*, 349, 113849

Cheng, A. F., Atchison, J., Kantsiper, B., et al. 2015, *AcAau*, 115, 262  
 Cheng, A. F., Rivkin, A. S., Michel, P., et al. 2018, *P&SS*, 157, 104  
 Ćuk, M., & Burns, J. A. 2005, *Icar*, 176, 418  
 Ćuk, M., Jacobson, S. A., & Walsh, K. J. 2021, *PSJ*, 2, 231  
 Ćuk, M., & Nesvorný, M. 2010, *Icar*, 207, 732  
 Davis, A. B., & Scheeres, D. J. 2020, *Icar*, 341, 113439  
 Davis, A. B., & Scheeres, D. J. 2021, GUBAS: General Use Binary Asteroid Simulator, Astrophysics Source Code Library, ascl:2107.013  
 Dotto, E., Della Corte, V., Amoroso, M., et al. 2021, *P&SS*, 199, 105185  
 Fahnestock, E., Cheng, A., & Richardson, D. C. 2018, in 42nd COSPAR Scientific Assembly (Pasadena, CA: JPL, NASA), S.3-5-18  
 Fahnestock, E. G., & Scheeres, D. J. 2006, *CeMDA*, 96, 317  
 Ferrari, F., Franzese, V., Pugliatti, M., Giordano, C., & Toppo, F. 2021, *AdSpR*, 67, 2010  
 Ferrari, F., Tasora, A., Masarati, P., & Lavagna, M. 2017, *Multibody. Syst. Dyn.*, 39, 3  
 Goldberg, H. R., Karatekin, O., Ritter, B., et al. 2019, in 33rd Annual AIAA/USU Small Satellite Conf. (Logan, UT: Utah State Univ.), <https://digitalcommons.usu.edu/smallsat/2019/all2019/73/>  
 Hirabayashi, M., Davis, A. B., Fahnestock, E. G., et al. 2019, *AdSpR*, 63, 2515  
 Hou, X., Scheeres, D. J., & Xin, X. 2017, *CeMDA*, 127, 369  
 Jacobson, S. A., & Scheeres, D. J. 2011, *ApJL*, 736, L19  
 Jacobson, S. A., Scheeres, D. J., & McMahon, J. 2013, *ApJ*, 780, 60  
 Levison, H., Olkin, C., Noll, K., & Marchi, S. 2017, European Planetary Science Congress 2017, *EPSC2017-963*  
 Levison, H. F., Olkin, C. B., Noll, K. S., et al. 2021, *PSJ*, 2, 171  
 Maciejewski, A. J. 1995, *CeMDA*, 63, 1  
 McMahon, J. W., & Scheeres, D. J. 2013, *CeMDA*, 115, 365  
 Meyer, A., Scheeres, D., Naidu, S., et al. 2021, AAS/Division of Dynamical Astronomy Meeting, 53, 405.06  
 Meyer, A. J., & Scheeres, D. J. 2021, *Icar*, 367, 114554  
 Michel, P., Küppers, M., Fitzsimmons, A., et al. 2021, *Europlanet Science Congress*, 15, EPSC2021-71  
 Naidu, S., Benner, L., Brozovic, M., et al. 2020, *Icar*, 348, 113777  
 Pravec, P., Scheirich, P., Kušnirák, P., et al. 2006, *Icar*, 181, 63  
 Pravec, P., Scheirich, P., Kušnirák, P., et al. 2016, *Icar*, 267, 267  
 Pravec, P., Scheirich, P., Scheeres, D., et al. 2021, IAA/Planetary Defense Conf. 7 (Vienna: UNOOSA)  
 Pravec, P., Wolf, M., & Sarounová, L. 1999, in IAU Coll. 173. Evolution and Source Regions of Asteroids and Comets, ed. J. Svoren et al. (Tatranska Lomnica, Slovak Republic: Astronomical Institute of the Slovak Academy of Sciences), 159  
 Quillen, A. C., LaBarca, A., & Chen, Y. 2021, arXiv:2107.14789  
 Richardson, D. C., Quinn, T., Stadel, J., & Lake, G. 2000, *Icar*, 143, 45  
 Scheeres, D. J. 2002, *CeMDA*, 83, 155  
 Scheeres, D. J. 2006, *CeMDA*, 94, 317  
 Scheeres, D. J. 2009, *CeMDA*, 104, 103  
 Scheeres, D. J., McMahon, J., Bierhaus, B., et al. 2020, AGUFM A252-01  
 Scheirich, P., & Pravec, P. 2009, *Icar*, 200, 531  
 Scheirich, P., Pravec, P., & Thomas, C. A. 2019, EPSC-DPS Joint Meeting EPSC-DPS2019-473  
 Steinberg, E., & Sari, R. 2011, *AJ*, 141, 55  
 Taylor, P. A., & Margot, J.-L. 2010, *CeMDA*, 108, 315  
 Taylor, P. A., & Margot, J.-L. 2014, *Icar*, 229, 418  
 Thomas, C., Rivkin, A., Moskovitz, N., et al. 2021, *LPSC*, 52, 2753  
 Tricarico, P. 2008, *CeMDA*, 100, 319  
 Tsiganis, K., Kueppers, M., Michel, P., et al. 2019, 21st EGU General Assembly 13147  
 Walsh, K. J., Richardson, D. C., & Michel, P. 2008, *Natur*, 454, 188  
 Werner, R. A., & Scheeres, D. J. 2005, *CeMDA*, 91, 337